



Enhanced mass transfer and optimized electronic structure on Pd–Ag nanoparticles embedded in mesoporous carbon for superior electro-oxidation

DePing Chen¹ · Mengjue Li¹ · Ying Chen¹ · Zhenyi Shao¹ · Yanhong Wei¹ · Yong Xian¹ · Xi Chuan Liu² · XianJun Ying³

Received: 19 March 2023 / Revised: 29 May 2023 / Accepted: 30 May 2023 / Published online: 28 June 2023
© The Author(s), under exclusive licence to Springer-Verlag GmbH Germany, part of Springer Nature 2023

Abstract

The development of economically viable anode catalysts for the alcohol oxidation reaction (AOR) has been a long-standing challenge in direct alcohol fuel cells (DAFCs). A series of Pd–Ag nanoparticles embedded in mesoporous carbon were fabricated in this study using a green approach that did not require the use of a surfactant, which exhibited better catalytic properties for AOR. Experiments and DFT calculations reveal that the d-band center of Pd is influenced by both strain and ligand effects, with the ligand effect predominating. The electrochemical studies demonstrated that the composite-optimized Pd–Ag alloy at a Pd/Ag molar ratio of 1:1 was the highest in terms of ethanol oxidation (EOR) and ethylene glycol oxidation (EGOR) catalytic activity. The mass activities of Pd₁Ag₁/MC for EOR and EGOR were 7921 mA mg⁻¹ and 11,520 mA mg⁻¹, respectively, which were 3.77 and 5.3 fold greater than Pd/C. The impressive performance of Pd₁Ag₁/MC catalyst could be attributed to the vital roles of the unique mesoporous structure of carbon sphere with abundant self-doping defect and the boosting effect of Ag (benefit from optimized d-band electronic structure and bi-functional mechanism). The present simple method of synthesizing low-cost, easy-to-use, and high-performance catalysts contributes to the exploration of the large-scale practical applications of direct alkaline alcohol fuel cells.

Keywords Pd–Ag alloy · D-band center · Ligand effect · Strain effect · Mesoporous carbon · Electro-oxidation

Introduction

The direct alcohol fuel cells (DAFCs) are good ways to cope with energy and environmental considerations [1, 2]. Ethanol and ethylene glycol-based biomass are considered a kind of sustainable and promising energy sources due to their low cost, high practical reliability, and low toxicity [3]. It is urgent to develop high-efficient catalysts for large-scale practical applications due to the slow kinetics and the intricate electrocatalytic process of the alcohol oxidation reaction (AOR). Currently, there have been significant efforts

made to improve the electrocatalytic activity of palladium (Pd)-based catalysts by developing alloy [4–8], hollow [9, 10], nanowires [11, 12], and core–shell structures [13, 14] with intriguing ligand and strain effects [15]. Among them, alloy nano-materials are rapidly developed due to their easy synthesis strategy and widespread use in application fields [16, 17]. According to the d-band theory proposed by Nørskov et al. [1], the combination of another relatively cheap oxyphilic metal with Pd has generally emerged as an efficient approach. It can not only tune the position of the d-band center of Pd but also reduce the dosage of Pd corresponding to the variation of Pd performance. Alloying Pd with another relatively cheap metal enables the optimization of surface and electronic structures with induced synergistic effects, thus enhancing the intrinsic activity of the catalyst, which has attracted extensive attention [18]. To date, the preparation and their catalytic activities of Pd-based alloys, such as Pd–Ag [13, 19–21], Pd–Cu [22, 23], Pd–Au [24], Pd–Ni [25–28], and Pd–Ge [29], have been evaluated. To our knowledge, in most synthetic methods of Pd-based alloy catalysts, stabilizers are used to avoid aggregation of Pd–Ag

✉ Mengjue Li
lmjue1@cdu.edu.cn

¹ School of Materials and Environmental Engineering, Chengdu Technological University, Chengdu 611730, China

² Department of Materials and Chemical Engineering, Yibin University, Yibin 644000, China

³ Chengdu Tool Research Institute Co, Ltd, Chengdu 610500, China

NPs [10, 14, 30], and it is difficult to remove the stabilizers that affect the catalytic activities of Pd-based alloy catalysts. Therefore, developing efficient Pd-based catalysts with a clean surface (no stabilizers are employed during the manufacturing process) for alcohol oxidation continues to be a key issue for the scientific community to commercialize DAFC [31].

In this work, the mesoporous carbon (MC) with high-specific surface area, self-doping defects, and mesoporous volume were introduced as support, and a series of Pd–Ag alloy nanoparticles with a clean surface supported on MC were synthesized through a simple metal precursor salt co-reduction method, with the merits of low-cost, environmentally friendly, and surfactant-free. Due to the defects of the mesoporous carbon that can anchor the nanoparticles, the Pd–Ag alloy nanoparticles of the same size were uniformly distributed on the MC, which was not only beneficial to enhance electro-catalysis but also conducive to understanding the alloying effects (study alloying effect without size effect). Following the addition of various amounts of Ag, the catalytic characteristics of Pd–Ag alloy nanoparticles were altered by modifying the molar Pd/Ag ratio, which resulted in a change in the d-band center (strain effect and ligand effect). Finally, the prepared catalysts' electrochemical characteristics in an alkaline electrolyte were investigated, and the electrochemical study revealed that the electrocatalytic activity and stability of the Pd₁Ag₁/MC significantly enhanced toward ethanol oxidation (EOR) and ethylene glycol oxidation (EGOR), which was attributable to the addition of Ag and the three-dimensional mesoporous carbon structure favorable for mass transfer. Due to this approach's exceptional simplicity and environmental friendliness, it was firmly believed that as-prepared Pd₁Ag/MC catalysts had significant promise for use as anode catalysts and in large-scale practical applications of direct alkaline fuel cells.

Experimental

Materials

Palladium chloride (PdCl₂, > 99.99%, Aladdin), silver nitrate (AgNO₃, > 99.99%, Aladdin), sodium borohydride (NaBH₄, 97.0%, KESHI), potassium hydroxide (KOH, Aladdin), Nafion, hydrochloric acid (HCl, 35–38%), anhydrous ethanol (C₂H₆O, 99.9%), span 80, resorcinol (C₆H₄(OH)₂, 99.5%), PEG-200, commercial Pd/C (20 wt %, Alfa Aesar), dichloromethane (CH₂Cl₂, > 99.9%), and formaldehyde solution (HCHO, 37.0–40.0%). Industrial white oil was purchased from Sichuan Mesto Petrochemical Technology Co., Ltd. All tests utilized water that was ultrapure with a resistivity of 18.23 MΩ·cm.

Support preparation

According to our previous report, mesoporous carbon (MC) was developed by inverting the micro-emulsion method [32]. In summary, resorcinol, formaldehyde, industrial white oil, PEG-200, and span 80 are mixed with ultrapure water in a proportional amount. The as-prepared materials were filtrated and washed multiple times with dichloromethane after standing for 12 h. Nanogel-prepared gels were then carbonized in a typical tube furnace under Ar for 4 h at 1223 K. The MC was then produced via a 2-h grinding of the material.

Catalyst preparation

Pd_xAg_y/MC (Pd₁Ag₃/MC, Pd₁Ag₁/MC, Pd₃Ag₁/MC, and Pd₅Ag₁/MC) catalysts were produced for different Pd and Ag molar ratios, with the total molar quantity of metal (Pd and Ag) regulated at 0.055 mM. The metal salt co-reduction approach was used to synthesize the MC-supported Pd–Ag catalysts [33]. Taking the preparation of Pd₁Ag₁/MC, for example, 0.0275 mM PdCl₂ and 0.0275 mM AgNO₃ were added into 50 mg MC powders simultaneously, ultrasonically dispersing the as-prepared solution at room temperature for 30 min. Following that, a dropwise application of NaBH₄ (1 mg/mL) was performed. The Pd₁Ag₁/MC catalyst was then completely washed with water and dried in vacuum at 50 °C. The contrast sample Pd/MC and Ag/MC catalysts were produced in a similar process without adding.

Characterizations

Transmission electron microscopy (TEM) was used to depict the morphologies of all of the catalysts studied (JEOL JEM-2100F system). The crystalline structure and particle size of the catalysts were measured using Cu k radiation patterns generated by X-ray diffraction (XRD, Bruker D8). The surface and binding energy information were characterized using X-ray photoelectron spectroscopy (XPS, ESCALAB Xi+). The AGILENT ICP-OES 730I instrument was used to measure the actual metal loading of the Pd_xAg/MC catalysts.

Electrochemical measurements

The electrochemical characterization of the three-electrode system was carried out using a CHI 660 workstation. The as-prepared catalysts were dispersed in 235 μL ultrapure

water, 250 μL anhydrous ethanol, and 15 μL 5% Nafion solution, respectively. Before beginning the experiment, the working electrode was prepared by smearing 5 μL ink onto its surface.

Computational methods

All simulated computations were carried out using Material Studio (2018). The exchange–correlation potential and energy were addressed using the generalized gradient approximation (GGA) form of the Perdew–Burke–Ernzerhof (PBE) exchange–correlation functional [34, 35]. To begin, the optimized lattice constants of Pd and Pd_1Ag_1 are 0.393 nm (Fig. 1a) and 0.409 nm (Fig. 1d), respectively. Figure 1b, e shows the structure of Pd(111) and $\text{Pd}_1\text{Ag}_1(111)$. After Ag atoms are introduced, the strain effect and ligand effect will be produced simultaneously; therefore, two kinds of virtual crystals are established to study strain effect and ligand effect, respectively. The two virtual surfaces are depicted in Fig. 1c, f, respectively. The lattice constant of the Pd_1Ag_1 crystal is fixed at 0.393 nm to generate the virtual crystal $\text{Pd}_1\text{Ag}_1\text{-L}$, and $\text{Pd}_1\text{Ag}_1\text{-L}(111)$ was sliced to investigate the effect of the ligand effect on the d-band center of Pd following Ag addition (the change of coordination environment of Pd). The lattice strain generated by the mismatch between the lattices of Pd and Ag atoms would affect the d-band center of Pd. To study the strain effect (tensile strain) produced by the introduction of Ag atoms, the virtual crystal

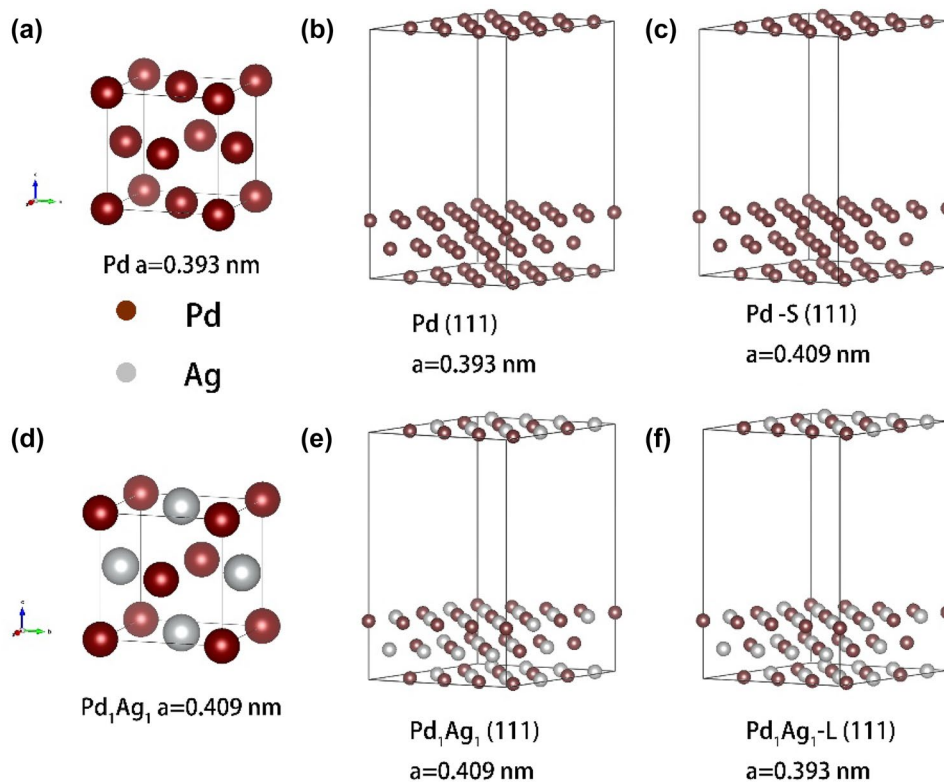
Pd-S was created by setting lattice constant to 0.409 nm (which is lattice constant of Pd crystal). All of the above surfaces were utilized to calculate the surface electrical structure by setting a three-layer metal slab with the top two layers loosened and the bottom layer fixed. A 15-Å vacuum zone was used to separate the slabs in the z-axis direction.

Results and discussion

DFT calculation

The d-band model [36–38] can well describe the adsorption and bonding in electrocatalytic reactions such as ORR, FAOR, and AOR. Therefore, the d-band center is commonly utilized as a significant descriptor to estimate the adsorbing capacity of molecules (O, OH, CO, or OOH, etc.) on metal catalysts. In this hypothesis, the downshifting of the d band center corresponds to a low level of interaction with intermediate compounds. Thus, by varying the position of the d-band center, it is possible to alter the adsorption energy between a metal catalyst and an intermediate molecular. Alloying the transition metals Ag with Pd allows the activity of Pd–Ag catalysts to be adjusted via strain and ligand effects, which are caused by the host lattice expansion due to lattice mismatch and the change in the chemical surrounding, respectively. The strain and ligand impacts on the d-band center have opposite effects in most cases; two virtual surfaces were developed for DFT calculations

Fig. 1 The calculation model of **a** Pd, **b** Pd (111), **c** Pd-S (111), **d** Pd_1Ag_1 , **e** Pd_1Ag_1 (111), **f** $\text{Pd}_1\text{Ag}_1\text{-L}(111)$



in order to distinguish between the effects of the strain and the influence of the ligand on the d-band center. The pure ligand effect of Pd_1Ag_1 was calculated by using lattice-strain-free virtual alloys (the virtual alloy surface denoted as $\text{Pd}_1\text{Ag}_1\text{-L}$ (111), $a=0.393$ nm), and the pure strain effect of Pd_1Ag_1 can be simulated in pure Pd by extending its lattice to a certain extent (the virtual surface denoted as Pd-S (111), $a=0.409$ nm). As shown in Fig. 2, the d-band center of virtual Pd-S (111) is higher (-1.95 eV) than that of Pd (111) (-2.08 eV), indicating the upshift of the d-band center, which attribute to the tensile stress introduced by the addition of Ag atom weakens the interaction between Pd atoms. The d-band center of $\text{Pd}_1\text{Ag}_1\text{-L}$ (111) is -2.85 eV, which is lower than Pd (111) (-2.08 eV), confirming that the alloying component Ag change the chemical surrounding of the Pd and resulting in downshifting the d-band center. Both the strain impact (tensile stress) and the ligand influence (coordination environment) have been taken into account to tune the d-band center in the surface of Pd_1Ag_1 (111). The strain effect leads the d-band center to move up ($\text{Pd}(111)=-2.08$ eV, $\text{Pd-S}(111)=-1.95$ eV), the ligand effect causes the d-band center to move down ($\text{Pd}(111)=-2.08$ eV, $\text{Pd}_1\text{Ag}_1\text{-L}(111)=-2.85$ eV), and the calculated d-band center of actual surface Pd_1Ag_1 (111) combining the strain effect and ligand effect is -2.79 eV, which is lower than that of Pd (111), indicating that the ligand effect is dominant in Pd_1Ag_1 (111). Based on the above DFT analyses, we conclude that the strain effects and ligand effects (coordination environment) caused by the incorporation of Ag result in a downshift of the d-band center (Fig. 3).

Crystal structure, morphology, and surface electronic state of $\text{Pd}_x\text{Ag}_y/\text{MC}$

Because ball milling introduces self-doping defects into the MC, which is advantageous for anchoring Pd–Ag NPs on the MC surface, the surface-clean $\text{Pd}_x\text{Ag}_y/\text{MC}$ products were synthesized by metal co-reduction without the use of a surfactant. According to the inductively coupled plasma measurements, the composition percentages of Pd to Ag in the $\text{Pd}_1\text{Ag}_3/\text{MC}$, $\text{Pd}_1\text{Ag}_1/\text{MC}$, $\text{Pd}_3\text{Ag}_1/\text{MC}$, and $\text{Pd}_5\text{Ag}_1/\text{MC}$ nano-catalysts are 3:1, 1:1, 3:1, and 5:1, respectively (Table S1), and these ratios are comparable to the atomic ratios of Pd and Ag in their metal precursors.

The bulk physical analyses of $\text{Pd}_1\text{Ag}_3/\text{MC}$, $\text{Pd}_1\text{Ag}_1/\text{MC}$, $\text{Pd}_3\text{Ag}_1/\text{MC}$, and $\text{Pd}_5\text{Ag}_1/\text{MC}$ were conducted using XRD (Fig. 4). As a contrast, the diffraction patterns of Ag/MC and Pd/MC synthesized under the same conditions are also exhibited in Fig. 4 (red line and black line, respectively). As shown in Fig. 4a, all of the samples show a typical face-centered-cubic (FCC) pattern. In the resulting Pd–Ag alloy samples, four distinct diffraction peaks in the 2θ range of 10 to 90° are found, suggesting that the catalysts are well-crystalline. The diffraction peak of the carbon (002) crystal plane is given to the peak at about 25° [39]. The Pd/MC sample shows distinctive peaks at 40.21° , 46.77° , 68.30° , and 82.33° , which correspond to the (111), (200), (220), and (311) planes of metallic Pd (Pd JCPDS:87–0639), space group: Fm-3 m (225), respectively. The peaks found for Ag/MC at 38.26° , 44.47° , 64.71° , and 77.73° are ascribed correspondingly to the metallic

Fig. 2 Projected ddensity-of-states (DOS) of $\text{Pd}_1\text{Ag}_1\text{-L}$ (111), Pd_1Ag_1 (111), Pd (111) and Pd-S (111)

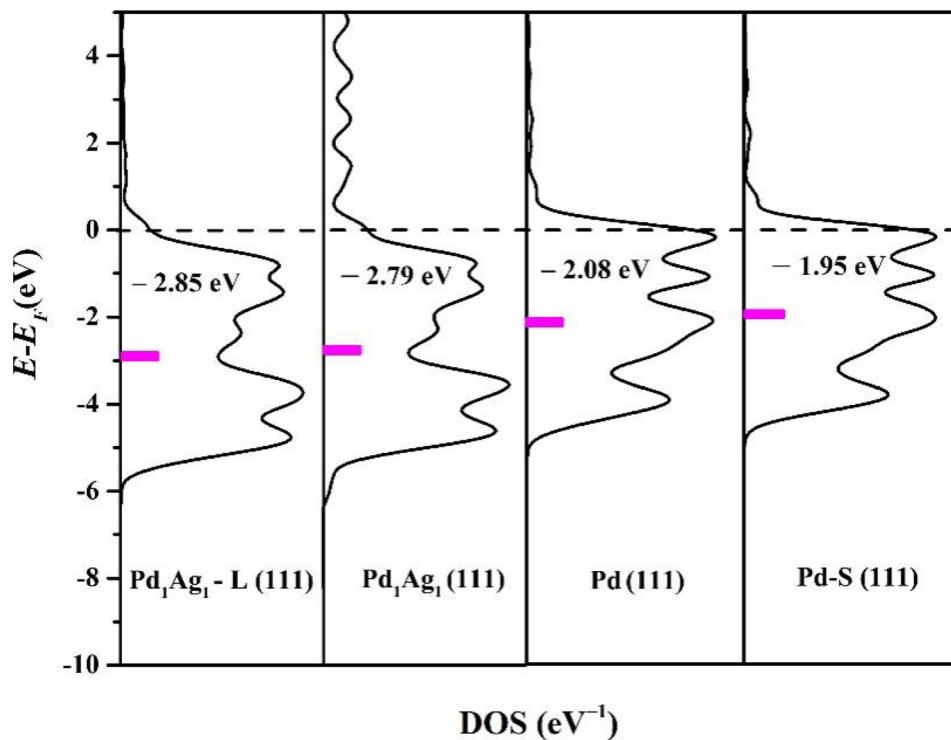
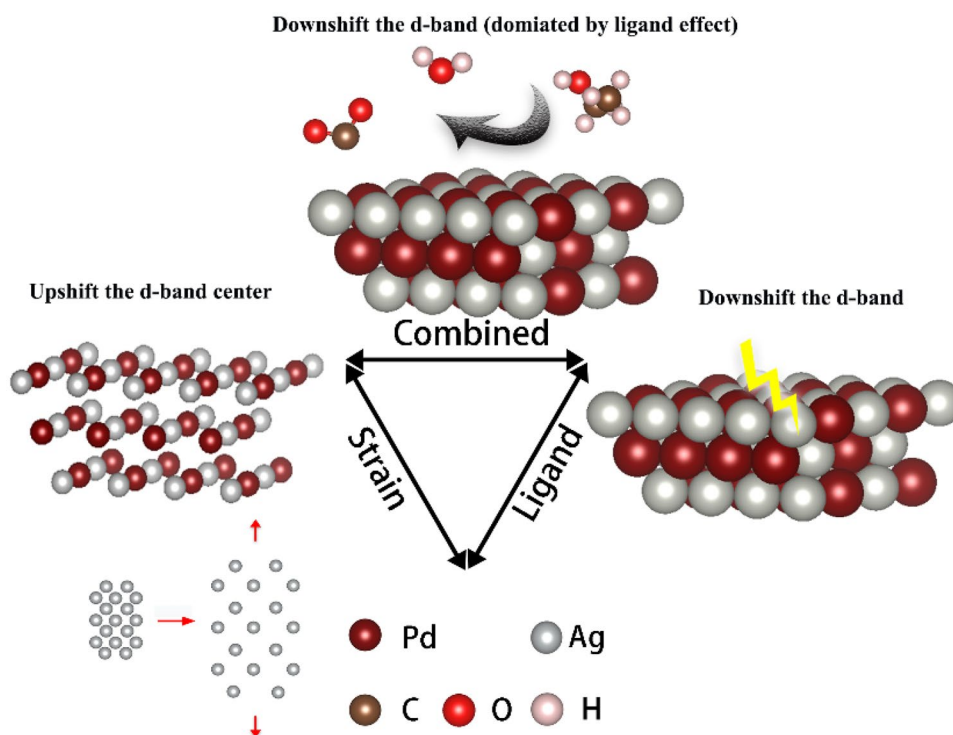


Fig. 3 Depiction of the lattice strain and ligand effects in the Pd_1Ag_1 alloy



Ag (111), (200), (220), and (311) planes (JCPDS:87–0719). In the bimetallic $\text{Pd}_x\text{Ag}_y/\text{MC}$ catalysts, diffraction peaks are found between the Pd/MC and the Ag/MC catalysts, which clearly demonstrates the alloy formation between the Pd and Ag metals. Figure 4b shows that as the Ag content increases, the 2θ of $\text{Pd}_x\text{Ag}_y/\text{MC}$ (111) plane shows more negative shifts, which is mainly attributed to the strain effect caused by lattice mismatch (Pd (0.393 nm) is mixed with Ag (0.422 nm)).

According to the deviation angle of the (111) crystal plane's diffraction characteristic peak in the XRD pattern

and the Scherrer equation [40], the lattice spacings for Pd/MC and $\text{Pd}_1\text{Ag}_1/\text{MC}$ are 0.222 nm and 0.228 nm, respectively. The above experimental results demonstrate that the strain effect caused by incorporating the metal Ag does change the spacing of the lattice fringes in the nanoparticles, resulting in average tensile stress of 3%.

The TEM images of $\text{Pd}_x\text{Ag}_y/\text{MC}$ ($\text{Pd}_1\text{Ag}_3/\text{MC}$, $\text{Pd}_1\text{Ag}_1/\text{MC}$, $\text{Pd}_3\text{Ag}_1/\text{MC}$, and $\text{Pd}_5\text{Ag}_1/\text{MC}$) catalysts and reference products (Pd/MC) are shown in Figs. 5a–d and 6a. Pd and Pd–Ag NPs with small-sized spherical morphologies are

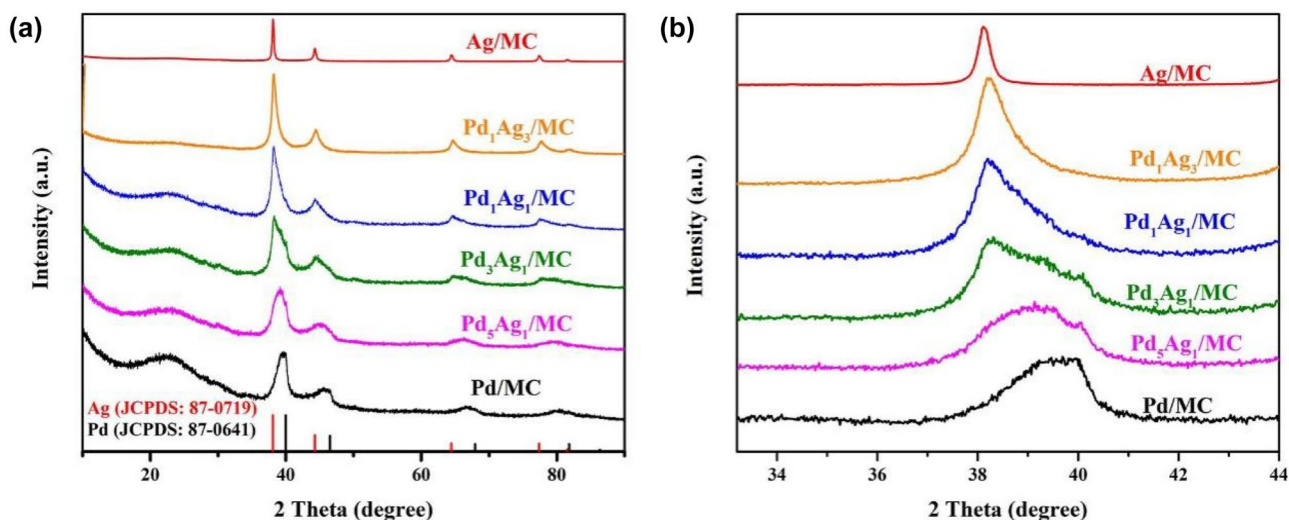


Fig. 4 a XRD patterns of $\text{Pd}_x\text{Ag}_y/\text{MC}$ catalysts. b The partially enlarged drawing of XRD

efficiently disseminated on the mesoporous carbon substrate due to the large surface area and mesoporous volume of MC. In addition, Figs. 5a-1-d-1 and 6b present the histograms of the catalyst size distribution calculated from the 50-nm scale TEM images. It can be found that the Pd NPs of Pd/MC, Pd₁Ag₃/MC, Pd₁Ag₁/MC, Pd₃Ag₁/MC, and Pd₅Ag₁/MC possess similar average sizes, which are approximately at 5.36 nm (Fig. 5a-1), 4.36 nm (Fig. 6b), 4.76 nm (Fig. 5b-1), 4.53 nm (Fig. 5c-1), and 4.54 nm (Fig. 5d-1), respectively. The TEM results indicate that the Ag contents in the Pd_xAg_y/MC catalysts have a negligible influence on their sizes. The inter-planar spacing in the corresponding Pd_xAg_y/MC catalyst HRTEM images is distinguished in Fig. 5a-2, b-2, c-2, and d-2 and Fig. 6c. According to the measurements in the insets of Fig. 5a-2-d-2 and Fig. 6c, the lattice spacings of Pd/MC, Pd₁Ag₃/MC, Pd₁Ag₁/MC, Pd₃Ag₁/MC, and Pd₅Ag₁/MC are 0.220 nm, 0.230 nm, 0.227 nm, 0.223 nm, and 0.221 nm, respectively. The lattice spacings of the Pd_xAg_y/MC catalysts are between that of the (111) plane of FCC Pd (0.22 nm) and the (111) plane of FCC Ag

(0.235 nm); the foregoing study further reveals the creation of the Pd–Ag alloy structure and the introduction of tensile stress in Pd_xAg_y/MC. The lattice spacings of Pd (111) in Pd_xAg_y/MC catalyst increases with the increase of Ag content, which is in accordance with the XRD analysis. As a characteristic catalyst, the scanning TEM (STEM) and EDS mapping techniques were used to further analyze Pd₁Ag₁/MC. As shown in Fig. 6d-g, Pd and Ag are uniformly distributed in the mesoporous carbon support, which further confirms that the obtained sample is a PdAg nano-alloy.

According to the results of XRD and TEM, the strain effect (tensile strain) is introduced into the alloy without changing the Pd crystal lattice, when the Ag atoms (a larger lattice constant than Pd) are incorporated into the lattice of the Pd [24, 30]. Meanwhile, as stated by the DFT calculation, the d-band center of Pd-S (111) and Pd (111) is –1.95 eV and –2.08 eV, respectively. Namely, the creation of the strain effect (tensile strain) results in an upshift of the d-band center, which is related to the increase in distance between Pd atoms and the weakening of the contact between

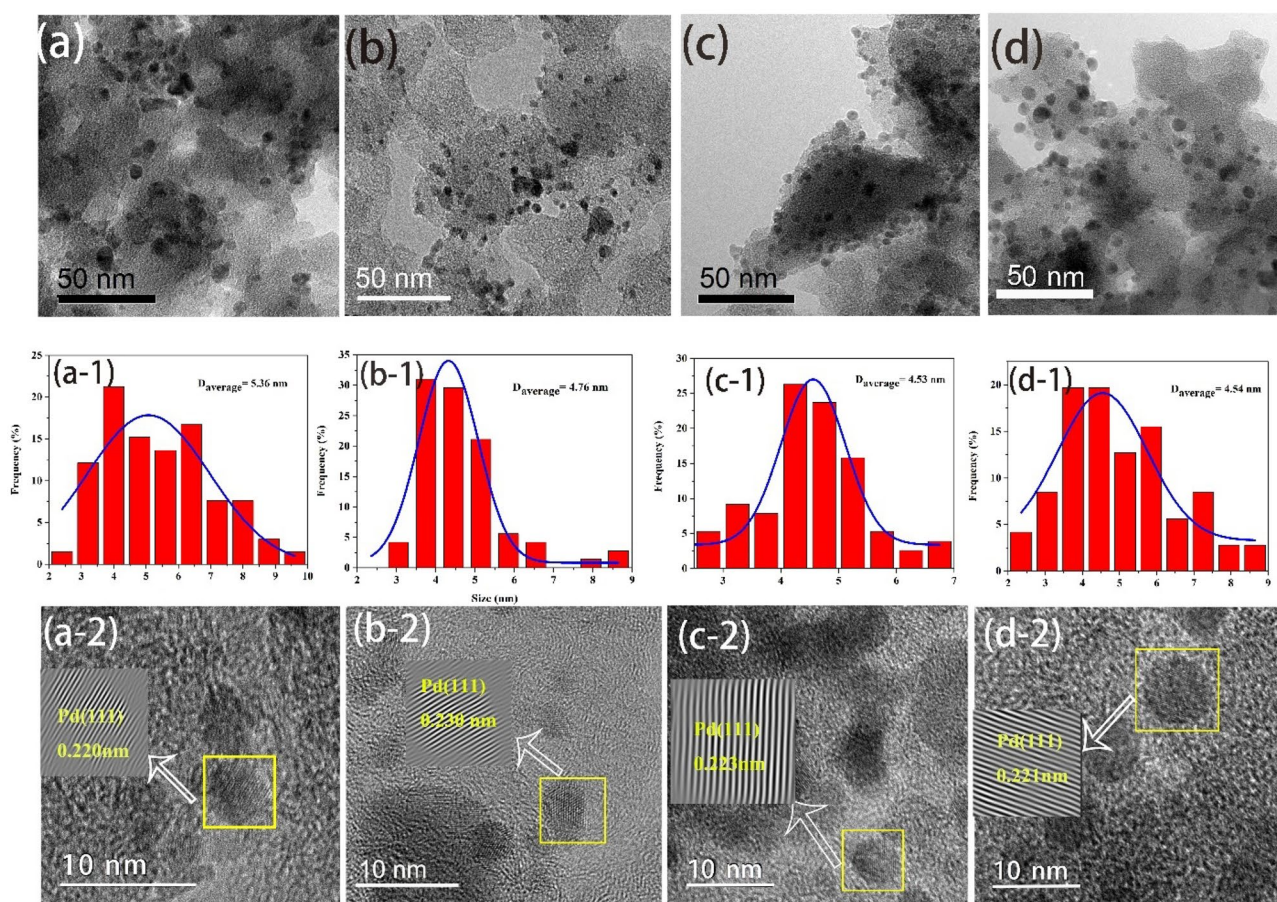
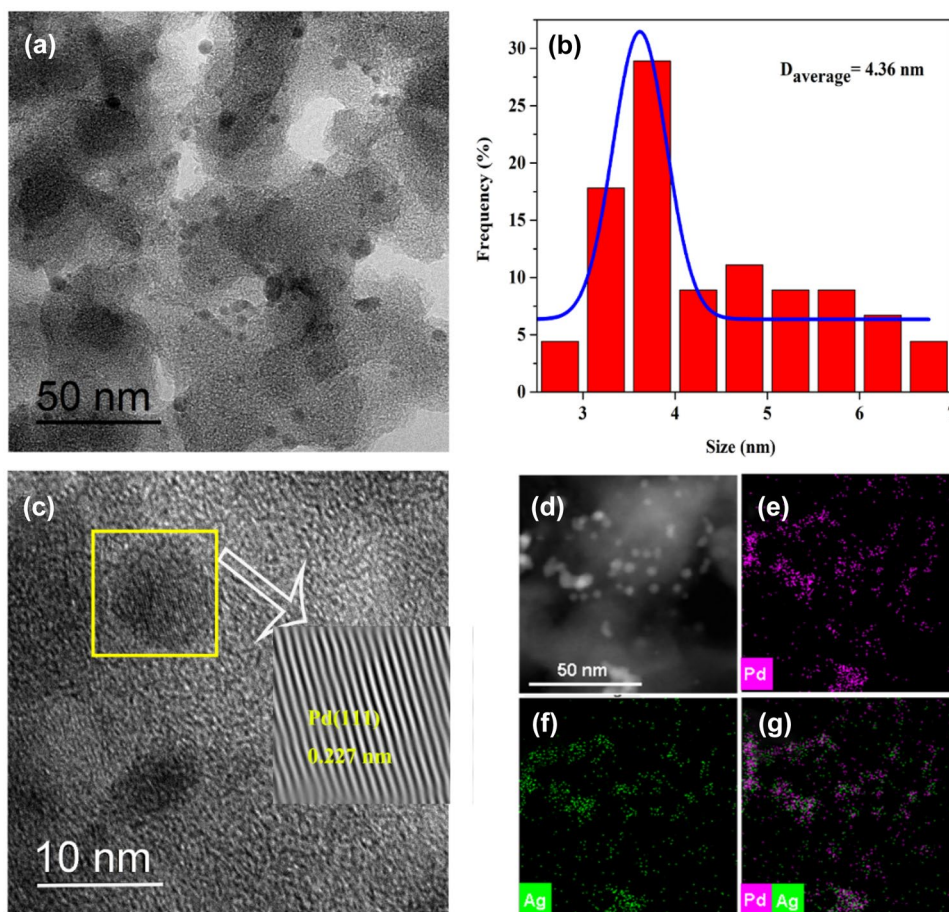


Fig. 5 The TEM images of Pd_xAg_y/MC. **a** Pd/MC, **b** Pd₁Ag₃/MC, **c** Pd₃Ag₁/MC, and **d** Pd₅Ag₁/MC, respectively. The size histograms of **a-1** Pd/MC, **b-1** Pd₁Ag₃/MC, **c-1** Pd₃Ag₁/MC, and **d-1** Pd₅Ag₁/MC.

The corresponding HRTEM images **a-2** Pd/MC, **b-2** Pd₁Ag₃/MC, **c-2** Pd₃Ag₁/MC, and **d-2** Pd₅Ag₁/MC. The inverse FFT images were shown in the insets of **(a-2 ~ d-2)**

Fig. 6 The TEM images of Pd₁Ag₁/MC. **a** The TEM images and **c** HRTEM image of Pd₁Ag₁/MC. **b** The particle size distribution of **a**. STEM **d** and EDS (e–g) elemental mappings of Pd₁Ag₁/MC



them. According to the d-band center hypothesis and our calculated results, the strain effect caused by the addition of Ag causes the d-band center of Pd to shift upward [41–43].

The electronic states of the Pd_xAg_y alloy NPs and the comparative samples on the mesoporous carbon were measured by XPS. In Fig. 7a, the peaks located at approximately 289 eV, 336 eV, 375 eV, and 531 eV are related to the C, Pd, Ag, and O elements, respectively. Only the peaks of Pd and C are observed in Pd/MC, while the peaks of Ag and C are detected in Ag/MC. The presence of Pd and Ag peaks in Pd₁Ag₃/MC, Pd₁Ag₁/MC, Pd₃Ag₁/MC, and Pd₅Ag₁/MC confirms the successful synthesis of the bimetallic Pd_xAg_y catalysts. The high-resolution XPS spectra of Pd_xAg_y/MC are shown in Fig. 7b, c, respectively. The two characteristic peaks of Pd/MC (orange-dotted line in Fig. 7b) are located at 340.7 eV (Pd⁰ 3d_{3/2}) and 335.4 eV (Pd⁰ 3d_{5/2}). Compared with those in the Pd/MC spectra, the Pd 3d orbitals of Pd_xAg_y/MC (Fig. 7b) shift to higher binding energy, and the deviation degree becomes greater with increasing Ag content (details obtained from Pd 3d and Ag 3d spectra are summarized in Table 1). In the Ag 3d spectra, the two characteristic peaks of Ag/MC (orange-dotted line orange in Fig. 7c) centered at 374.6 eV and 368.5 eV match to Ag⁰ 3d_{3/2} and Ag⁰ 3d_{5/2}. The binding energy of Pd_xAg_y/MC

catalysts is shifted to lower binding energy than those of Ag/MC. According to previous reports, the positive shift of the Pd⁰ peak and the negative shift of Ag⁰ are assigned to the electronic structure change between Pd and Ag atoms.

These findings show that there is a high electronic correlation between Pd and Ag when making a Pd–Ag alloy and that the d-bands of the Pd and Ag atoms overlap, resulting in electron transfer from Pd to Ag, which is consistent with previous literature investigations [24, 44]. According to the d-band center theory, the positive change in the Pd 3d binding energy associated with the downshift of the d-band center could diminish Pd's adsorption capacity for detrimental intermediated species, resulting in an increase in its catalytic activity [45].

The valence band spectra (VBS) of Pd_xAg_y/MC and Pd/MC are shown in Fig. 7d. The density of states (DOS) of Pd_xAg_y/MC exhibits a clear increase and is far away from the Fermi level, indicating that the d-band center is downshifted compared to Pd/MC. The d-band center of Pd₁Ag₃/MC, Pd₁Ag₁/MC, Pd₃Ag₁/MC, Pd₅Ag₁/MC, and Pd/MC are located at –5.28, –4.76, –4.20, –4.16, and –3.84 eV, respectively. Compared with Pd/MC, it can be seen that the d-band center of Pd_xAg_y/MC deviates from the Fermi level, and the degree of departure

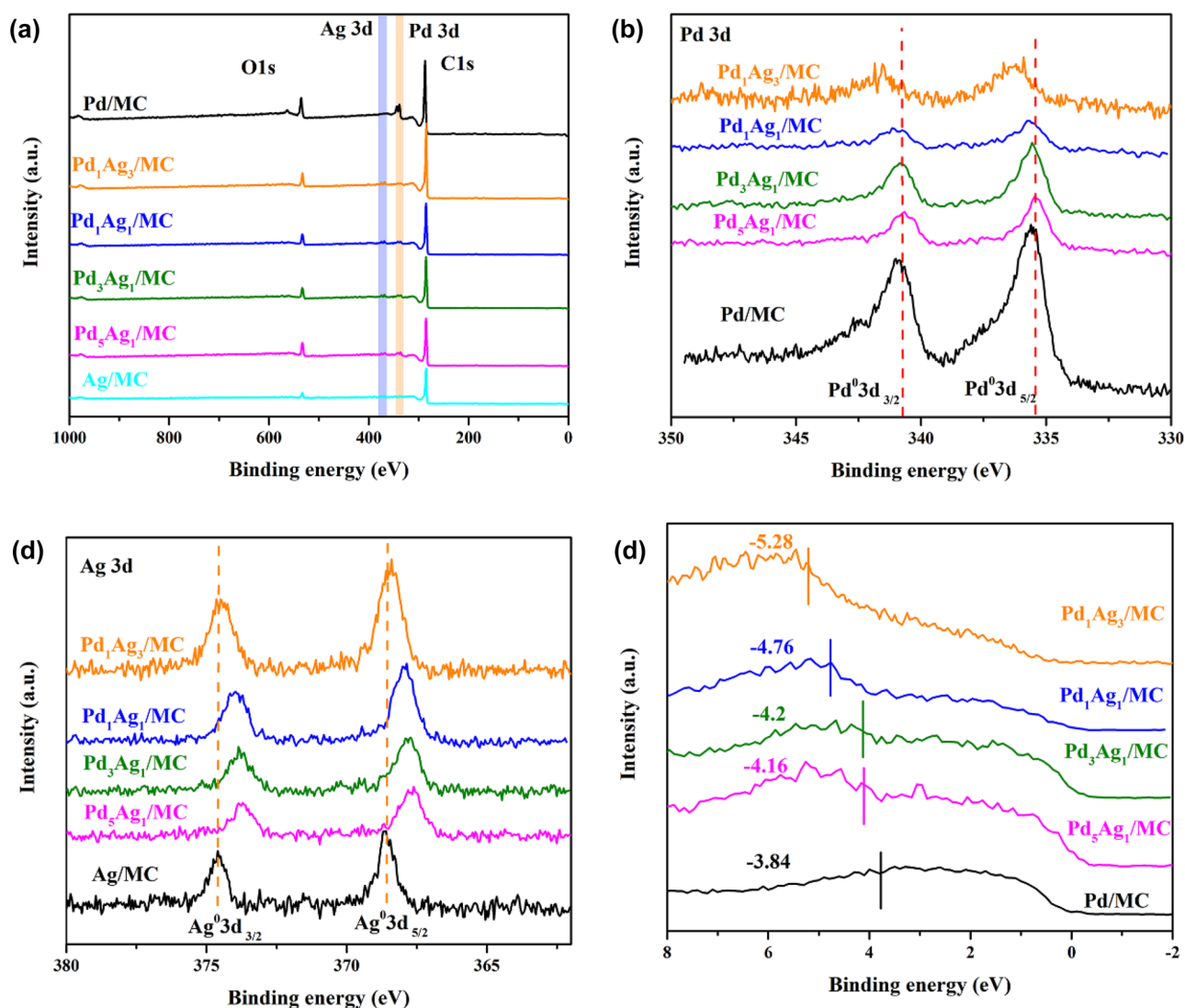
Table 1 XPS analysis of the catalysts

Sample	aE_B (eV) Ag ⁰		aE_B (eV) Pd ⁰		aE_B (eV) Pd ²⁺	
	Ag ⁰ 3d _{5/2}	Ag ⁰ 3d _{3/2}	Pd ⁰ d _{5/2}	Pd ⁰ d _{3/2}	Pd ²⁺ 3d _{5/2}	Pd ²⁺ 3d _{3/2}
Pd/MC	/	/	335.4	340.7	336.8	342.1
Ag/MC	368.5	374.6	/	/	/	/
Pd ₁ Ag ₃ /MC	368.4	374.5	336.1	341.5	337.6	343.1
Pd ₁ Ag ₁ /MC	367.9	373.9	335.6	340.9	337.5	342.8
Pd ₃ Ag ₁ /MC	367.8	373.8	335.5	340.8	337.4	342.7
Pd ₅ Ag ₁ /MC	367.7	373.7	335.4	340.7	337.3	342.7

^aE_B is the binding energy

risers as the Ag concentration increases. The DFT calculated d-band centers of Pd₁Ag₃, Pd₁Ag₁, Pd₃Ag₁, Pd₅Ag₁, and Pd are −3.42 eV, −2.79 eV, −2.28 eV, −2.16 eV, and −2.08 eV, respectively (Fig. 8). The DFT

calculated d-band center data differ from experimental VBS d-band centers, but the patterns of d-band center change and increase of DOS around Fermi level match the experimental XPS results in Fig. 7d with the increasing

**Fig. 7** XPS spectra of Pd_xAg_y/MC catalyst and comparison samples. **a** XPS survey spectra, **b** Pd 3d, **c** Ag 3d XPS, **d** valence band spectra of catalyst

of Ag content. DFT calculations are corroborated by our results from our valence band study, which shows that the inclusion of Ag significantly changes the d band and eventually causes its center to move down.

To summarize, when Ag is introduced into Pd to form the Pd–Ag alloy, the ligand effect (which results in the d-band center downshifting due to a strong electron interaction between Pd and Ag) and the strain impact (the increase in distance between Pd atoms and the weakening of the contact between them result in the d-band center upshifting) have an effect on the d-band center, and the d-band center of $\text{Pd}_x\text{Ag}_y/\text{MC}$ is predominantly governed by the ligand effect, which results in the catalyst's d-band center shifting downward.

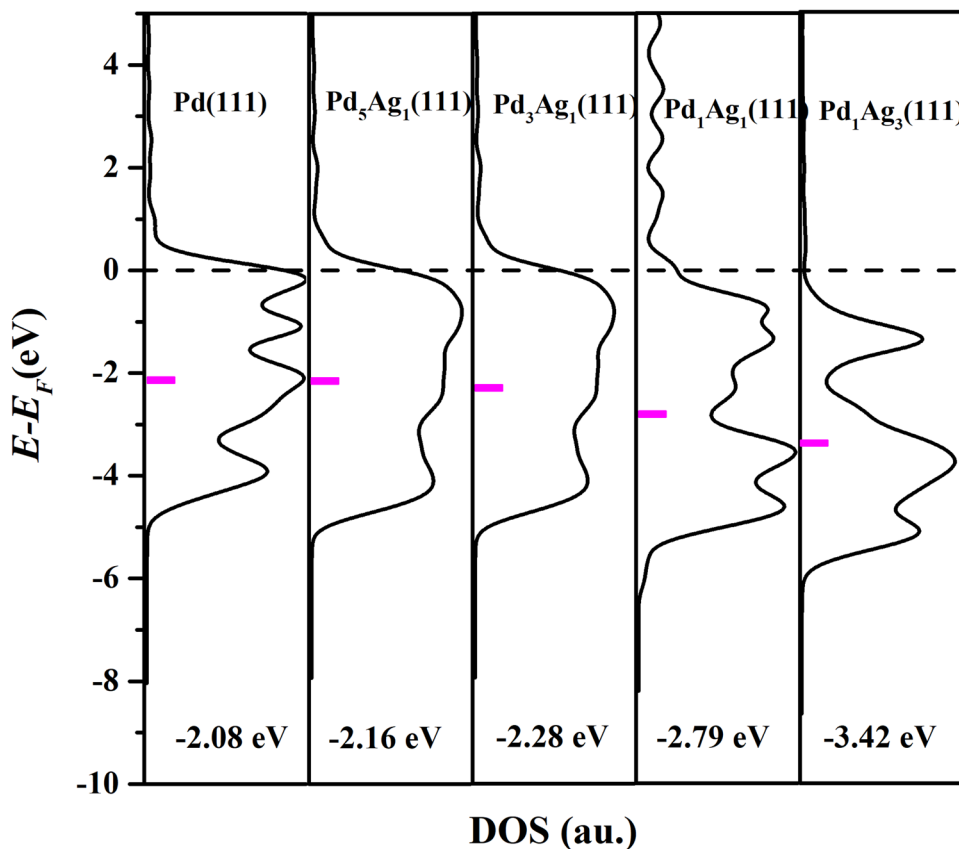
Electrocatalytic performance for $\text{Pd}_x\text{Ag}_y/\text{MC}$

According to these experimental data and DFT calculations, after the addition of Ag atoms, the d-band center of $\text{Pd}_1\text{Ag}_1/\text{MC}$ shifts away from the Fermi level, which benefits the desorption of reaction intermediates and the release of active sites directly. On the other hand, Ag can increase the adsorption capacity of OH^- and facilitate to the oxidation of intermediate product via its bi-functional catalytic mechanism. On the other hand, through the bi-functional catalytic

mechanism, Ag can promote the adsorption of OH^- and the oxidation of intermediates [30]. Thus, as a result, when compared to the Pd/MC product, it can be predicted that the $\text{Pd}_1\text{Ag}_1/\text{MC}$ catalysts prepared in this work have a good electrocatalytic performance for the anodic oxidation reaction.

The electrochemically active surface area (ECSA) is a useful metric for determining the amount of active sites on a catalyst surface. The CV curves for Pd/MC, $\text{Pd}_1\text{Ag}_3/\text{MC}$, $\text{Pd}_1\text{Ag}_1/\text{MC}$, $\text{Pd}_3\text{Ag}_1/\text{MC}$, $\text{Pd}_5\text{Ag}_1/\text{MC}$, and Pd/C catalysts in 1.0 M KOH are shown in Fig. 9a. All curves show that the current peaks attribute to the reduction of palladium oxides around -0.3 V in the reverse scanning. In accordance with the increasing Ag concentration, the current reduction peak of PdO increases, implying that the surface of $\text{Pd}_x\text{Ag}_y/\text{MC}$ contains more active sites. The ECSA of the catalysts is calculated by Eq. 1, where Q is the quantification of electric charges related to PdO reduction, and $\text{Pd}_{\text{loading}}$ is Pd content on the working electrode. Herein, the ECSA of $\text{Pd}_1\text{Ag}_1/\text{MC}$ catalysts is $311.15 \text{ m}^2 \text{ g}^{-1}$, which is higher than that of $\text{Pd}_1\text{Ag}_3/\text{MC}$ ($124.92 \text{ m}^2 \text{ g}^{-1}$), $\text{Pd}_3\text{Ag}_1/\text{MC}$ ($107.1 \text{ m}^2 \text{ g}^{-1}$), $\text{Pd}_5\text{Ag}_1/\text{MC}$ ($67.96 \text{ m}^2 \text{ g}^{-1}$), Pd/MC ($76.34 \text{ m}^2 \text{ g}^{-1}$), and Pd/C ($62.29 \text{ m}^2 \text{ g}^{-1}$). The excellent ECSA of $\text{Pd}_1\text{Ag}_1/\text{MC}$ is due to the uniform dispersion of Pd–Ag nanoparticles with a small size on the mesoporous carbon substrate; furthermore, the large ECSA benefits from the appropriate composition

Fig. 8 Projected d density-of-states (DOS) of $\text{Pd}_1\text{Ag}_3(111)$, $\text{Pd}_1\text{Ag}_1(111)$, $\text{Pd}_3\text{Ag}_1(111)$, $\text{Pd}_5\text{Ag}_1(111)$, and Pd(111)



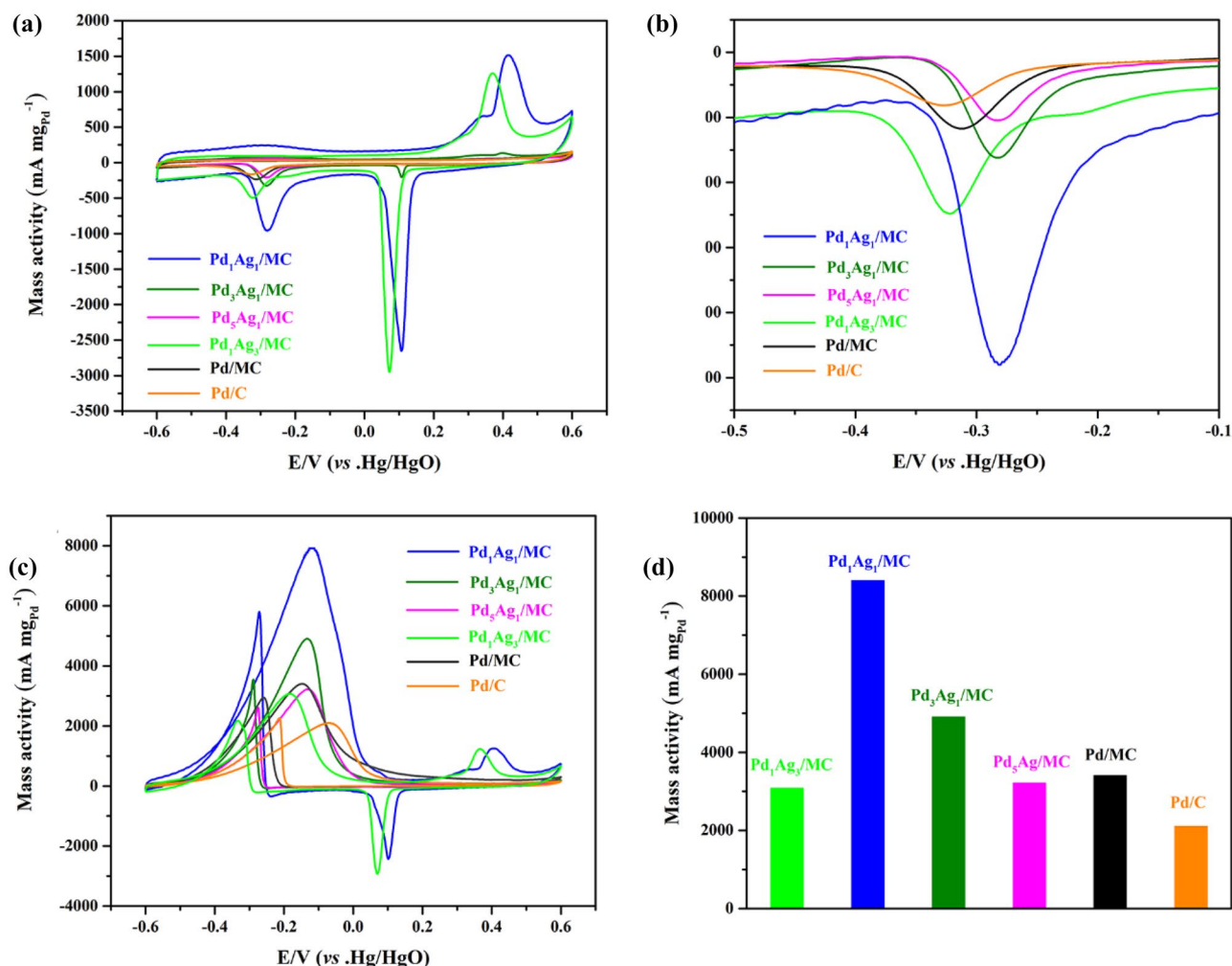


Fig. 9 CV curves of Pd_xAg_y/MC, Pd/MC and Pd/C in **a** 1 M KOH solution and **c** 1 M KOH + 1 M CH₃CH₂OH solution, **b** The enlarged curve of (a), **d** The histograms of mass activities of Pd_xAg_y/MC, Pd/MC and Pd/C

of the Pd–Ag alloy. Besides, the peaks (corresponding to the reduction of PdO) of Pd_xAg_y/MC is more negative than those of Pd/MC and Pd/C nanocatalysts, which indicates that the Pd_xAg_y/MC catalyst can reduce the PdO at a higher potential. The peak behaviors of the Pd_xAg_y/MC indicate a shift in the electronic structure of Pd upon Ag inclusion. The electrical structure of Pd was altered after Ag was added, as shown by the XPS and XRD spectra above.

$$\text{ESCA}(\text{m}^2 \text{g}^{-1}) = \frac{Q(C) \times 0.1}{0.405(\text{mC cm}^{-2}) \times \text{Pd}_{\text{loading}}(\text{g})} \quad (1)$$

The CV measurements of Pd_xAg_y/MC catalysts were conducted to test their catalytic activities toward EOR after activating. Figure 9c illustrates that all CV curves have two anode peaks, one is ethanol oxidation in the forward scanning peak, and the other anode peak appears in the reverse scanning, associating with partially oxidized carbonaceous

species accumulated in the front scan [46]. The mass of Pd on the electrode is utilized to normalize the forward sweep peak currents of the Pd_xAg_y/MC catalysts. As illustrated in Fig. 9d, Pd_xAg_y/MC samples perform better in terms of EOR than Pd/C catalysts. The mass activity of Pd₁Ag₁/MC and Pd/C are 7921 mA mg⁻¹ and 2100 mA mg⁻¹, respectively. Fig. S1 shows the cyclic voltammetry curve of Ag/MC tested in 1 M KOH+1 M EtOH. It can be seen from the figure that there is no ethanol oxidation peak of Ag/MC, indicating that Ag has no catalytic activity on ethanol oxidation reaction. Additionally, our findings were compared to previously published literature to validate the superior activity of Pd₁Ag₁/MC (Table S2). The mass activity of Pd₁Ag₁/MC catalysts toward EOR is relatively high compared with the electrocatalyst previously reported.

To gain a better understanding of the EOR transfer behavior on the Pd₁Ag₁/MC catalyst, a series of CV curves were obtained at various scan rates. Figure 10a shows CV curves

for Pd₁Ag₁/MC of catalytic EOR in 1.0 M KOH and 1.0 M ethanol at scanning rates of 10 to 50 mV s⁻¹. With the rise in the scan rate, the EOR oxidation peak current steadily increases, while the summit potential is slightly pushed to the positive value. Based on the results presented in Fig. 10b, it appears that the peak current for ethanol oxidation is linearly proportional to the square root of the scanning rate ($v^{1/2}$), suggesting that mass transport regulation is dominant in the ethanol oxidation process. The long-term stability of Pd₁Ag₁/MC catalysts is also important in assessing their performance. To determine the electrocatalyst stability of the Pd_xAg_y/MC, Pd/MC, and Pd/C catalysts, we performed chronoamperometry tests in a 1 M KOH + 1 M CH₃CH₂OH solution at potential of -0.1 V with saturated Ar for 2100s. The mass activity-time curves presented in Fig. 11 show that as time increases, the present values of the Pd_xAg_y/MC, Pd/MC, and Pd/C samples are plainly declining due to intermediate poisoning of the catalyst active sites. At 2100s, the current density of Pd₁Ag₁/MC is 411.2 mA mg_{Pd}⁻¹, which is higher than that of the Pd/C catalyst (36.6 mA mg_{Pd}⁻¹); this demonstrates that the stability of the Pd₁Ag₁/MC catalyst is greater in long-term usage than that of Pd/C [8, 47]. The improvement in Pd₁Ag₁/MC stability owes to the inclusion of Ag that can decrease the adsorption capacity of intermediate species by altering the d-band center of catalysts; furthermore, Ag atoms can increase the adsorption capacity of OH⁻ on its surface, oxidation of toxic species, and the release of additional active areas during the process of electro-oxidation based on bi-functional processes [45, 48].

Analogously, the electrocatalytic activities of the Pd₁Ag₁/MC for EGOR were also examined (Fig. 12a). The mass activity histograms of Pd₁Ag₁/MC, Pd/MC, and Pd/C toward EGOR are shown in Fig. 12b. The mass activity of Pd₁Ag₁/MC (11,520 mA mg⁻¹_{Pd}) is 5.3 times larger

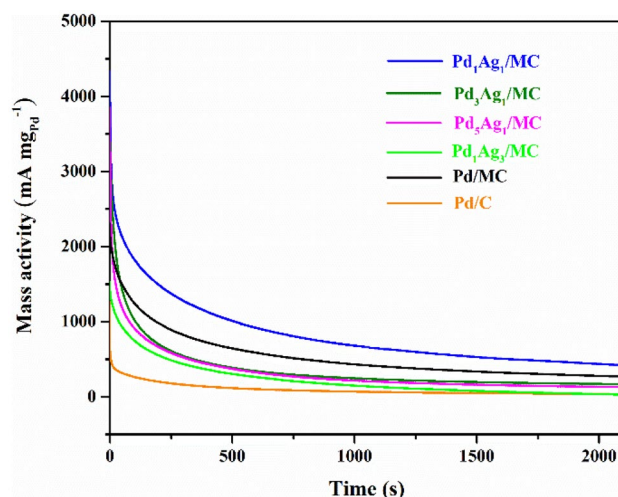


Fig. 11 Chronoamperometric curves of Pd₁Ag₁/MC, Pd/MC, and Pd/C catalysts in 1 M KOH + 1 M CH₃CH₂OH

than that of Pd/C (2170 mA mg⁻¹_{Pd}). In addition, the results were compared with previously reported literature, and it was confirmed that Pd₁Ag₁/MC had higher EGOR mass activity than the previously reported electrocatalysts (Table S3). Figure 12c illustrates an appropriate linear relationship between the EGOR oxidation peak current and the square root of scan rates ($v^{1/2}$), which displays that the transfer behavior of EGOR is controlled by mass transport. According to the chronoamperometry measurements (Fig. 12d), Pd₁Ag₁/MC catalysts had greater current densities than Pd/MC and Pd/C at first, indicating that high surface active sites are exposed in Pd₁Ag₁/MC due to the uniform-dispersion of metal NPs on MC. From 200 to 2100s, the current densities of Pd₁Ag₁/MC catalyst is

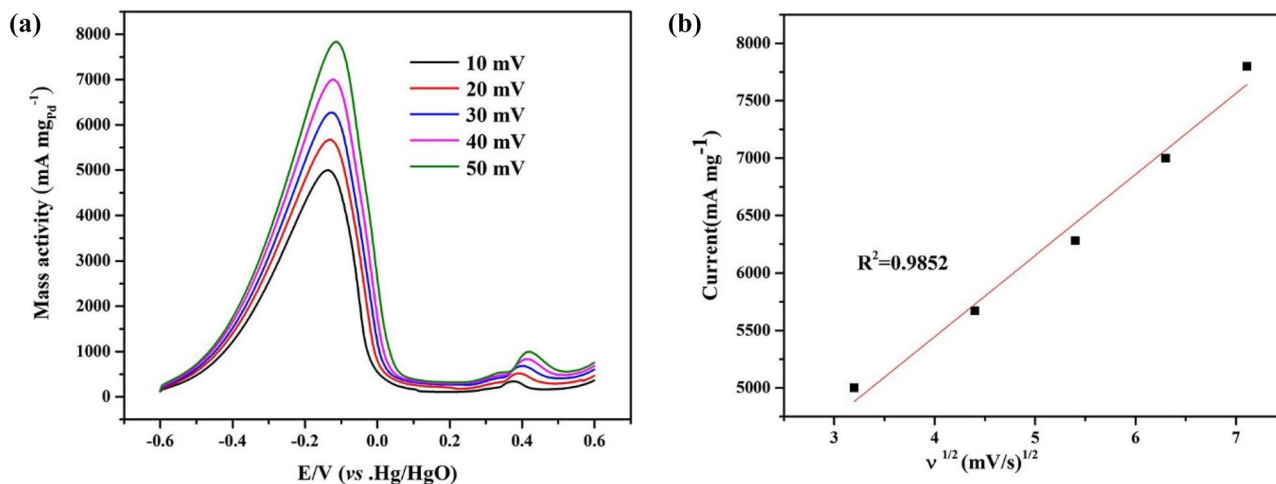


Fig. 10 **a** LCV curves of Pd₁Ag₁/MC in 1 M KOH + 1 M CH₃CH₂OH at different scan rate. **b** The linear relationship between I and $v^{1/2}$

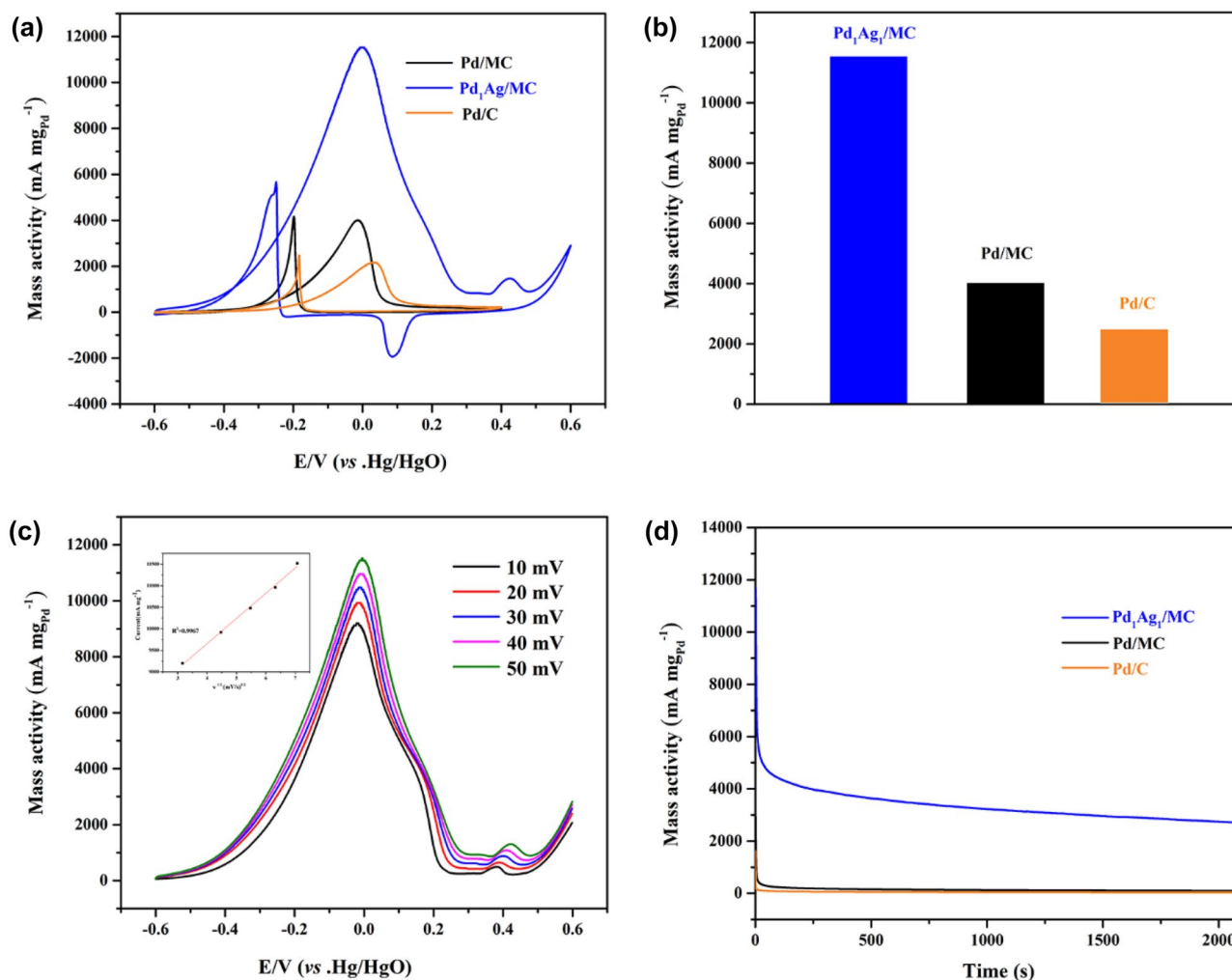


Fig. 12 CV curves of Pd₁Ag₁/MC, Pd/MC and Pd/C in **a** 1 M KOH + 1 M ethylene glycol, **b** The histograms for mass activities of Pd₁Ag₁/MC, Pd/MC and Pd/C. **c** LCV curve of Pd₁Ag₁/MC with different scanning rate in 1 M KOH + 1 M EG solution, the relationship between

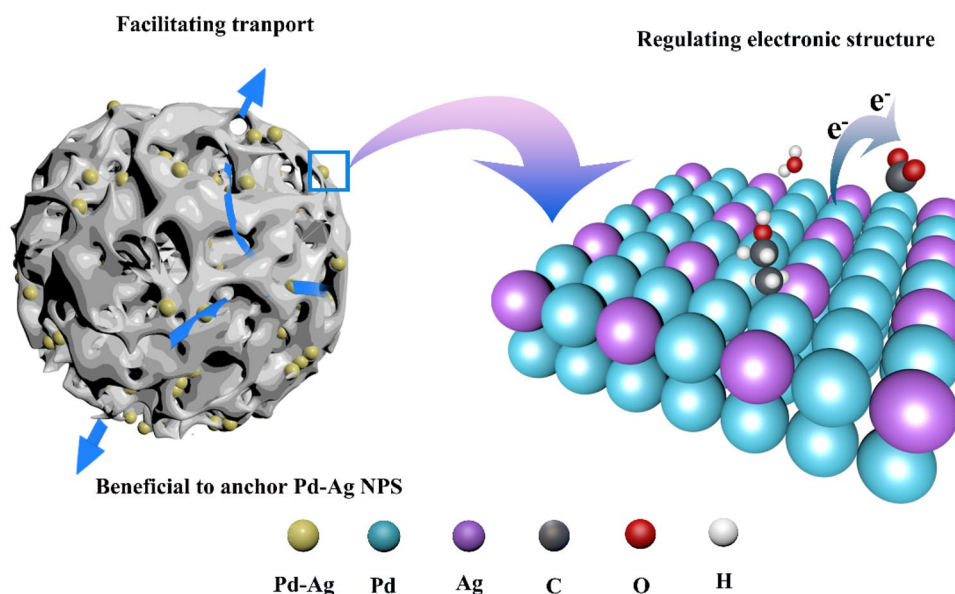
current and the square root of the scanning rate is shown in insert of figure (c). **d** Chronoamperometric curves of Pd₁Ag₁/MC, Pd/MC and Pd/C catalysts in 1 M KOH + 1 M EG

practically stable, indicating efficient elimination of CO-poisoning compounds from Pd surface active sites. At 2100s, the current density values of Pd₁Ag₁/MC are bigger than the Pd/MC and Pd/C, implying that Pd₁Ag₁/MC has better long-term endurance toward EOR.

As confirmed above, the performance improvement of Pd_xAg_y/MC on the electro-oxidation reaction of ethanol and ethylene glycol can be attributed to synergistic effects of uniquely self-doped mesoporous nanostructure advantages and modulated electronic structure of Ag (Fig. 13). To begin, the formation of Pd–Ag alloy on 3D mesoporous carbon nanostructures with self-doping defects resulted in a large number of surface active sites, which were not only resistant

to agglomeration and dissolution but also promoted mass and electron transport during the electro-oxidation reaction. Moreover, the synergistic effect after the addition of Ag would improve catalytic activity; the reasons are as follows: (1) based on the bi-functional mechanism, Pd–Ag alloys tend to produce oxygen-containing substances under alkaline conditions, which can promote the oxidation of intermediate species and the release of additional active sites, and (2) the d-band center of catalyst is effectively downshifted (dominated by ligand effects) to weaken the affinity between Pd and oxygen-containing intermediates, thereby releasing active sites on the Pd surface, resulting in a favorable electronic environment for electro-oxidation reaction.

Fig. 13 Schematic representation of Pd₁Ag₁/MC catalysts' increased electrocatalytic activity mechanisms



Conclusion

In conclusion, a series of Pd–Ag alloys supported on mesoporous carbon were successfully manufactured using a simple and environmentally friendly approach. The strain effect and ligand effect were confirmed using HRTEM, XRD, and XPS data to establish the production of Pd–Ag alloy on the mesoporous. The electrochemical activity of Pd_xAg_y/MC catalysts with different Pd/Ag atomic ratios was investigated. As a consequence, the as-prepared Pd_xAg_y/MC catalyst had outstanding electrocatalytic performance for EOR, while the optimized Pd₁Ag₁/MC catalyst demonstrated the most remarkable electrocatalytic activity, much more than that of Pd/MC and some others described in the literature. Moreover, it also has very efficient electrocatalytic performance for EGOR. Because of the synergy between Pd and Ag, the Pd₁Ag₁/MC catalyst has better electrocatalytic performance than the Pd/MC catalyst. Meanwhile, based on the d-band theory, Ag can modify the electronic structure of Pd and result in lower adsorption capacity for intermediates, as evidenced by XPS measurements and DFT calculations. According to our findings, the high-performance Pd₁Ag₁/MC produced using an easy and environmentally friendly method could prove to be a viable electro-catalyst in the future, assisting in the commercialization of DAFC.

Supplementary Information The online version contains supplementary material available at <https://doi.org/10.1007/s10008-023-05561-3>.

Author contribution De Ping Chen: Implementing, writing, modifying. Ying Chen, Yanhong Wei, Yong Xian, Xi Chuan Liu: Discussing, remarking. Li Mengjue: Discussing, supervising.

Funding This work was financially supported by the Natural Science Foundation of Sichuan Province (2023NSFSC0913).

References

- Chen A, Ostrom C (2015) Palladium-based nanomaterials: synthesis and electrochemical applications. *Chem Rev* 115:11999–12044
- Debe MK (2012) Electrocatalyst approaches and challenges for automotive fuel cells. *Nature* 486:43–51
- Antolini EJJ (2007) Catalysts for direct ethanol fuel cells. *J Power Sources* 170:1–12
- Zhu C, Guo S, Dong S (2013) Rapid, general synthesis of PdPt bimetallic alloy nanosponges and their enhanced catalytic performance for ethanol/methanol electrooxidation in an alkaline medium. *Chemistry* 19:1104–1111
- Fu S, Zhu C, Du D, Lin Y (2015) Facile one-step synthesis of three-dimensional Pd–Ag bimetallic alloy networks and their electrocatalytic activity toward ethanol oxidation. *ACS Appl Mater Interfaces* 7:13842–13848
- Kiyani R, Rowshanzamir S, Parnian M JJE (2016) Nitrogen doped graphene supported palladium-cobalt as a promising catalyst for methanol oxidation reaction: synthesis, characterization and electrocatalytic performance 113:1162–1173
- Wang Y, Zou S, Cai W-B (2015) Recent advances on electro-oxidation of ethanol on Pt- and Pd-based catalysts: from reaction mechanisms to catalytic materials. *Catalysts* 5:1507–1534
- Bianchini C, Shen PK (2009) Palladium-based electrocatalysts for alcohol oxidation in half cells and in direct alcohol fuel cells. *Chem Rev* 109:4183–4206
- Chen D, Cui P, He H, Liu H et al (2014) Highly catalytic hollow palladium nanoparticles derived from silver@silver–palladium core–shell nanostructures for the oxidation of formic acid. *J Power Sources* 272:152–159
- Gao F, Zhang Y, Song P, Wang J et al (2019) Self-template construction of Sub-24 nm Pd Ag hollow nanodendrites as highly efficient electrocatalysts for ethylene glycol oxidation. *J Power Sources* 418:186–192
- Zhang S, Liu K, Liu Z, Liu M et al (2021) Highly strained Au–Ag–Pd alloy nanowires for boosted electrooxidation of biomass-derived alcohols. *Nano Lett* 21:1074–1082
- Lu Y, Chen W (2011) PdAg alloy nanowires: facile one-step synthesis and high electrocatalytic activity for formic acid oxidation. *ACS Catal* 2:84–90

13. Bian W, Chen F, Li Z, Kou B et al (2021) Surface phase stability of PdAg core-shell nanoalloys in oxidizing atmospheres and its relevance to surface atomic charge. *J Alloys Compd* 869:159345–159357
14. Huang L, Yang J, Wu M, Shi Z et al (2018) PdAg@Pd core-shell nanotubes: superior catalytic performance towards electrochemical oxidation of formic acid and methanol. *J Power Sources* 398:201–208
15. Xia Z, Guo S (2019) Strain engineering of metal-based nanomaterials for energy electrocatalysis. *Chem Soc Rev* 48:3265–3278
16. Liu S, Zhang C, Yuan L, Bao J et al (2013) Component-controlled synthesis of small-sized Pd-Ag bimetallic alloy nanocrystals and their application in a non-enzymatic glucose biosensor. *Sens Actuators B* 187:549–556
17. Zhang L, Wang H, Li X, Xia F et al (2015) One-step synthesis of palladium-gold-silver ternary nanoparticles supported on reduced graphene oxide for the electrooxidation of methanol and ethanol. *Electrochim Acta* 172:42–51
18. Farsadrooh M, Noroozifar M, Modarresi-Alam AR, Saravani H (2019) Sonochemical synthesis of high-performance Pd@CuNWs/MWCNTs-CH electrocatalyst by galvanic replacement toward ethanol oxidation in alkaline media. *Ultrason Sonochem* 51:478–486
19. Yin B, Zhao E, Hua X, Wang K et al (2020) Ultrafine PdAg nanoparticles immobilized on nitrogen-doped carbon/cerium oxide for superior dehydrogenation of formic acid. *New J Chem* 44:2011–2015
20. Chowdhury SR, Kanti Bera K, Ray A, Bera P et al (2021) Synergistic catalytic activity of palladium-silver alloy nanoparticle for anodic oxidation of ethanol in alkali. *Int J Hydrogen Energy* 46:14212–14224
21. Lović JD, Elezović NR, Jović BM, Zabinski P et al (2018) Electrodeposited AgPd alloy coatings as efficient catalysts for the ethanol oxidation reaction. *Int J Hydrogen Energy* 43:18498–18508
22. Zhu C, Shi Q, Fu S, Song J et al (2016) Efficient synthesis of MCu (M = Pd, Pt, and Au) aerogels with accelerated gelation kinetics and their high electrocatalytic activity. *Adv Mater* 28:8779–8783
23. Yang N, Zhang Z, Chen B, Huang Y et al (2017) Synthesis of ultrathin PdCu alloy nanosheets used as a highly efficient electrocatalyst for formic acid oxidation. *Adv Mater* 29:1700769
24. Lam BTX, Chiku M, Higuchi E, Inoue H (2015) Preparation of PdAg and PdAu nanoparticle-loaded carbon black catalysts and their electrocatalytic activity for the glycerol oxidation reaction in alkaline medium. *J Power Sources* 297:149–157
25. Tan JL, De Jesus AM, Chua SL, Sanetuntikul J et al (2017) Preparation and characterization of palladium-nickel on graphene oxide support as anode catalyst for alkaline direct ethanol fuel cell. *Appl Catal A* 531:29–35
26. Zhang Z, Xin L, Sun K, Li W (2011) Pd–Ni electrocatalysts for efficient ethanol oxidation reaction in alkaline electrolyte. *Int J Hydrogen Energy* 36:12686–12697
27. Kottayintavida R, Gopalan NK (2020) Pd modified Ni nanowire as an efficient electro-catalyst for alcohol oxidation reaction. *Int J Hydrogen Energy* 45:8396–8404
28. Chen L, Lu L, Zhu H, Chen Y et al (2017) Improved ethanol electrooxidation performance by shortening Pd–Ni active site distance in Pd–Ni–P nanocatalysts. *Nat Commun* 8:14136–14145
29. Rajamani AR, Ashly PC, Dheer L, Sarma SC et al (2019) Synergistic effect of Ni-substituted Pd₂Ge ordered intermetallic nanocomposites for efficient electrooxidation of ethanol in alkaline media. *ACS Appl Energy Mater* 2:7132–7141
30. Ren F, Xu L, Xu H, Tang Y et al (2021) One-pot synthesis of alloyed PdAg networks as efficient catalysts of ethylene glycol electro-oxidation in alkaline media. *J Alloys Compd* 854:157075–157083
31. Lin C, Lu L, Zhu H, Chen Y et al (2017) Improved ethanol electrooxidation performance by shortening Pd–Ni active site distance in Pd–Ni–P nanocatalysts 8:14136–14145
32. Chen DP, Liu XC, Liu XD, Yuan L et al (2021) Pd nanoparticles on self-doping-defects mesoporous carbon supports for highly active ethanol oxidation and ethylene glycol oxidation. *Int J Hydrogen Energy* 46:30455–30466
33. Ranjbar Bahadori S, Hart R, Hao Y-W (2020) Synthesis of cobalt, palladium, and rhenium nanoparticles. *Tungsten* 2:261–288
34. Miao B, Wu Z-P, Xu H, Zhang M et al (2019) DFT studies on the key competing reaction steps towards complete ethanol oxidation on transition metal catalysts. *Comput Mater Sci* 156:175–186
35. Al-Odail F, Mazher J, Abuelela AM (2018) A density functional theory study of structural, electronic and magnetic properties of small Pd_nAg (n = 1–8) clusters. *Comput Theor Chem* 1125:103–111
36. Bligaard T, Nørskov JK (2007) Ligand effects in heterogeneous catalysis and electrochemistry. *Electrochim Acta* 52:5512–5516
37. Hammer B, Morikawa Y, Nørskov JK (1996) CO chemisorption at metal surfaces and overlayers. *Phys Rev Lett* 76:2142–2144
38. Xin H, Vojvodic A, Voss J, Nørskov JK et al (2014) Effects of d-band shape on the surface reactivity of transition-metal alloys. *Phys Rev B* 89:867–875
39. Douk AS, Saravani H, Farsadrooh M, Noroozifar M (2019) An environmentally friendly one-pot synthesis method by the ultrasound assistance for the decoration of ultrasmall Pd-Ag NPs on graphene as high active anode catalyst towards ethanol oxidation. *Ultrason Sonochem* 58:104616–104624
40. Kang YS, Choi D, Cho J, Park H-Y et al (2020) Highly active and durable ordered intermetallic PdFe electrocatalyst for formic acid electrooxidation reaction. *ACS Applied Energy Materials* 3:4226–4237
41. Gan L, Heggen M, Rudi S, Strasser P (2012) Core-shell compositional fine structures of dealloyed Pt(x)Ni(1-x) nanoparticles and their impact on oxygen reduction catalysis. *Nano Lett* 12:5423–5430
42. Cui C, Gan L, Heggen M, Rudi S et al (2013) Compositional segregation in shaped Pt alloy nanoparticles and their structural behaviour during electrocatalysis. *Nat Mater* 12:765–771
43. Chen G, Kuttiyiel KA, Su D, Li M et al (2016) Oxygen reduction kinetics on Pt monolayer shell highly affected by the structure of bimetallic AuNi cores. *Chem Mater* 28:5274–5281
44. Wakisaka M, Mitsui S, Hirose Y, Kawashima K et al (2006) Electronic structures of Pt-Co and Pt-Ru alloys for CO-tolerant anode catalysts in polymer electrolyte fuel cells studied by EC-XPS. *J Phys Chem B* 110:23489–23496
45. Hong W, Wang J, Wang E (2014) Synthesis of porous PdAg nanoparticles with enhanced electrocatalytic activity. *Electrochem Commun* 40:63–66
46. Liang ZX, Zhao TS, Xu JB, Zhu LD (2009) Mechanism study of the ethanol oxidation reaction on palladium in alkaline media. *Electrochim Acta* 54:2203–2208
47. Hu G, Nitze F, Barzegar HR, Sharifi T et al (2012) Palladium nanocrystals supported on helical carbon nanofibers for highly efficient electro-oxidation of formic acid, methanol and ethanol in alkaline electrolytes. *Electrochim Acta* 209:236–242
48. Fu S, Zhu C, Du D, Lin Y (2015) Facile one-step synthesis of three-dimensional Pd-Ag bimetallic alloy networks and their electrocatalytic activity toward ethanol oxidation. *ACS Appl Mater Interfaces* 7:13842–13848

Publisher's Note Springer Nature remains neutral with regard to jurisdictional claims in published maps and institutional affiliations.

Springer Nature or its licensor (e.g. a society or other partner) holds exclusive rights to this article under a publishing agreement with the author(s) or other rightsholder(s); author self-archiving of the accepted manuscript version of this article is solely governed by the terms of such publishing agreement and applicable law.